On the Importance of the Work Function and Electron Carrier Density of Oxide Electrodes for the Functional Properties of Ferroelectric Capacitors

Jun Wang, Minh Duc Nguyen, Nicolas Gauquelin, Johan Verbeeck, Minh Thanh Do, Gertjan Koster, Guus Rijnders, and Evert Houwman*

It is important to understand the effect of the interfaces between the oxide electrode layers and the ferroelectric layer on the polarization response for optimizing the device performance of all-oxide ferroelectric devices. Herein, the effects of the oxide $La_{0.07}Ba_{0.93}SnO_3$ (LBSO) as an electrode material in an $PbZr_{0.52}Ti_{0.48}O_3$ (PZT) ferroelectric capacitor are compared with those of the more commonly used $SrRuO_3$ (SRO) electrode. SRO (top)/PZT/SRO (bottom), SRO/PZT/LBSO, and SRO/PZT/2 nm SRO/LBSO devices are fabricated. Only marginal differences in crystalline properties, determined by X-ray diffraction and scanning transmission electron microscopy, are found. High-quality polarization loops are obtained, but with a much larger coercive field for the SRO/PZT/LBSO device. In contrast to the SRO/PZT/SRO device, the polarization decreases strongly with increasing field cycling. This fatigue problem can be remedied by inserting a 2 nm SRO layer between PZT and LBSO. It is argued that strongly increased charge injection into the PZT occurs at the bottom interface, because of the low PZT/LBSO interfacial barrier and the much lower carrier density in LBSO, as compared with that in SRO, causing a low dielectric constant, depleted layer in LBSO. The charge injection creates a trapped space charge in the PZT, causing the difference in fatigue behavior.

Ferroelectric thin films have been widely studied to understand their fundamental physics and for many applications using their ferroelectric nonvolatile memory and fast switching

characteristics.[1] Recently, memristor-like devices, such as ferroelectric resistive memory showing neuron-like adaptive characteristics, have also received great attention.[2–7] It is important to study the performance of these ferroelectric devices, such as the operating voltage, operating speed, and working stability.[8,9]

Lead zirconate titanante $Pb(Zr_{0.52}, Ti_{0.48})O_3$ (PZT) is one of the best known materials for ferroelectric nonvolatile memory applications, because of its large polarization and high Curie temperature.[10,11] Typically, a layer of ferroelectric material is sandwiched between a pair of electrodes to realize the functionalities in capacitors. The influence of the electrode materials on the polarization properties is important and has been discussed extensively. Using metal electrodes, commonly Pt, the switchable polarization of the PZT significantly decreases under prolonged switching cycling (fatigue behavior). Various models, such as oxygen vacancies accumulation at the metal–PZT interface and domain wall pinning, have been proposed to understand this polarization degradation.[12–14]

With the development of thin-film material growth techniques, such as pulsed laser deposition, all-oxide, epitaxial, heterostructure-based, and ferroelectric devices can be fabricated.[15] Conductive oxide materials, such as $SrRuO_3$ (SRO) and $LaNiO_3$(LNO), are now widely used as electrodes in the laboratory to solve the fatigue problem. A commonly used explanation for the fatigue resistance is that oxide electrodes act as oxygen vacancy sinks (or an oxygen reservoir) that suppress oxygen vacancy accumulation.[16–18]

Several theoretical models provide explanations for the interface-induced phenomena in the polarization response of ferroelectric thin films. For example, a passive layer (causing incomplete polarization screening), a depletion layer at the interface, and charge injection from the electrode into the ferroelectric layer all have effects on the coercive field, voltage offset, and working stability of ferroelectric devices.[19–22] In all-oxide devices, different types of contacts can be created using oxide electrode materials with different work functions and carrier concentrations. It is of great importance for device performance to understand the effect of different interface contacts on

Dr. J. Wang, Dr. M. D. Nguyen, M. T. Do, Prof. G. Koster, Prof. G. Rijnders, Dr. E. Houwman
MESA+ Institute for Nanotechnology
University of Twente
PO Box 217, 7500 AE Enschede The Netherlands
E-mail: e.p.houwman@utwente.nl

Dr. N. Gauquelin, Prof. J. Verbeeck
Electron Microscopy for Materials Science (EMAT)
University of Antwerp
2020 Antwerp, Belgium

The ORCID identification number(s) for the author(s) of this article can be found under https://doi.org/10.1002/pssr.201900520.

the polarization response of ferroelectric devices and the relation with intrinsic characteristics of different oxide electrode materials.

Recently, La-doped $BaSnO_3$ (LBSO), which has a cubic perovskite structure, has gained a lot of attention because of its optical transparency, its high electron mobility at room temperature, and its chemical stability.[23,24] Since the lattice constant of 4.11 Å is quite well matched with those of PZT ($a = 4.046$ Å and $c = 4.145$ Å),[25] LBSO is a promising electrode material for PZT ferroelectric devices. As LBSO is an optical transparent material, understanding the performance of PZT devices with a LBSO electrode may also provide us the opportunity to use nonvolatile ferroelectric memories in optical applications.[26] It is expected to prevent the buildup of a strain field caused by misfit dislocations and may replace the often used expensive (SRO).[27] The conductivity of this material arises from the partial replacement of Ba^{2+} by La^{3+}, changing the average charge on the Sn sites. This changes the material from an insulator to a metal, by shifting the Fermi level from the top of the oxygen p bands into the conduction band formed by the hybridized s and p states of the Sn and O atoms, respectively.[28] It has a wide bandgap of 3.2 eV, a low carrier concentration of about 4×10^{20} cm^{-3}, and a work function of about 4.4 eV.[29–31] SRO is a metal with a work function of 5.2 eV.[32] It has a very high carrier concentration of about 2×10^{22} cm^{-3},[33] two orders higher than that of LBSO. The differences between SRO and LBSO are expected to give rise to different interface contacts at the PZT/SRO and PZT/LBSO interfaces, respectively.

Oxide heterostructures SRO (top)/PZT/SRO (bottom) and SRO/PZT/LBSO were fabricated on TiO_2-terminated (001)-oriented $SrTiO_3$ (STO) substrates using pulsed laser deposition.[34] To further clarify the role of the interface on polarization switching and the fatigue of the PZT thin films, for some devices a thin SRO layer (2 nm) between the PZT and the bottom electrode LBSO (SRO/PZT/2 nm SRO/LBSO) was introduced. The interface between the PZT thin film grown on SRO has been well studied in previous works,[35,36] which show that atomic interdiffusion is absent. However, there are no reports on the properties of the interface between PZT and a LBSO electrode. High-resolution scanning transmission electron microscopy (HRSTEM) was performed on the SRO/PZT/LBSO device. High crystallinity of the LBSO and PZT thin films and a quite sharp, ordered PZT/LBSO interface with a transition region less than or equal to about two unit cells are observed in the STEM image, as shown in **Figure 1**a. Chemical maps obtained by electron energy loss spectroscopy (EELS) of the Ti $L_{2,3}$, La $M_{4,5}$, and Sn $M_{2,3}$ edge for the region in the red rectangle of Figure 1a are shown in Figure 1b with the simultaneously acquired annular dark field (ADF) image. The sharp interface, indicated by the green arrows, clearly evidences that there is no perceptible atomic interdiffusion at the interface between LBSO and PZT. The width of the transition region in an EELS line scan is about 1 nm, which is caused by the limited resolution of the electron beam. The initial growth layer of PZT on the LBSO shows hardly any growth defects, which is to be expected from the relatively small lattice mismatch. A similar growth is obtained for PZT on the 2 nm SRO layer on the LBSO, as SRO is fully epitaxially strained to the LBSO (see Figure S1, Supporting Information).
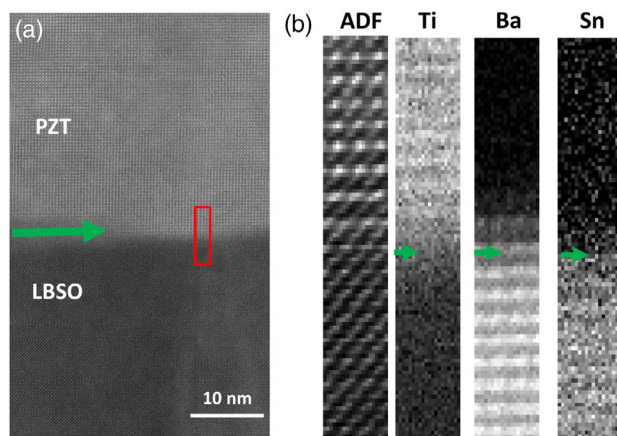

Figure 1. a) STEM image at low magnification showing PZT/LBSO structure. b) Chemical maps obtained by EELS of the Ti $L_{2,3}$, Ba $M_{4,5}$, and Sn $M_{2,3}$ edges for the region in the red rectangle of (a) with the simultaneously acquired ADF image.

Figure 2a,c shows X-ray diffraction (XRD) scans of SRO/PZT/SRO and SRO/PZT/LBSO thin films, respectively. The (00l) peaks from each layer are clearly present. In Figure 2a, the peak of SRO (002) corresponds to the bottom electrode. Because the SRO top electrode is strained by PZT, causing a smaller out-of-plane lattice constant, the SRO top electrode reflection peak shifts to higher angle and is visible as a shoulder on the left side of the STO peak (Figure 2c). As a large part of the SRO top electrode layer was etched away to make the capacitor structure, the intensity of the corresponding peak is much reduced compared with that of the bottom electrode. The XRD spectra indicate that all the PZT thin films are epitaxially grown with (001) orientation and also show that no secondary phase is formed. The insets give the corresponding rocking curves of the PZT (002) reflections. The full width at half maximum (FWHM) is 0.14° for the PZT on the SRO bottom electrode (Figure 2a) and 0.13° for the PZT on the LBSO bottom electrode (Figure 2c), indicating that all PZT thin films have a high crystallinity. To further characterize the crystalline quality and strain state of the PZT thin films, reciprocal space maps on the (103) reflections of SRO/PZT/SRO and SRO/PZT/LBSO thin films are shown in Figure 2b,d respectively. As shown in Figure 2b, the bottom SRO electrode is coherently grown on the STO substrate with an in-plane, coherently strained lattice constant $a = 3.905$ Å (for bulk SRO, the pseudocubic lattice constant is 3.93 Å). The LBSO bottom electrode, shown in Figure 2d, is nearly fully relaxed on the STO substrate with an in-plane lattice constant $a = 4.098$ Å, almost equal to that of bulk LBSO. Due to the large in-plane lattice mismatch between PZT and strained SRO, the PZT thin film on the SRO bottom electrode is fully relaxed by defects in the first few unit cell layers and has an (average) measured in-plane lattice constant $a_m = 4.057$ Å (index m for measured) and an (average) out-of-plane lattice constant $c_m = 4.113$ Å ($c_m/a_m = 1.014$) (Figure 2b). The PZT thin film on LBSO has an in-plane lattice constant $a_m = 4.079$ Å and an out-of-plane lattice constant $c_m = 4.105$ Å ($c_m/a_m = 1.006$) (Figure 2d). The XRD scan and reciprocal space map of the SRO/PZT/2 nm SRO/LBSO device are shown in Figure 2e,f.
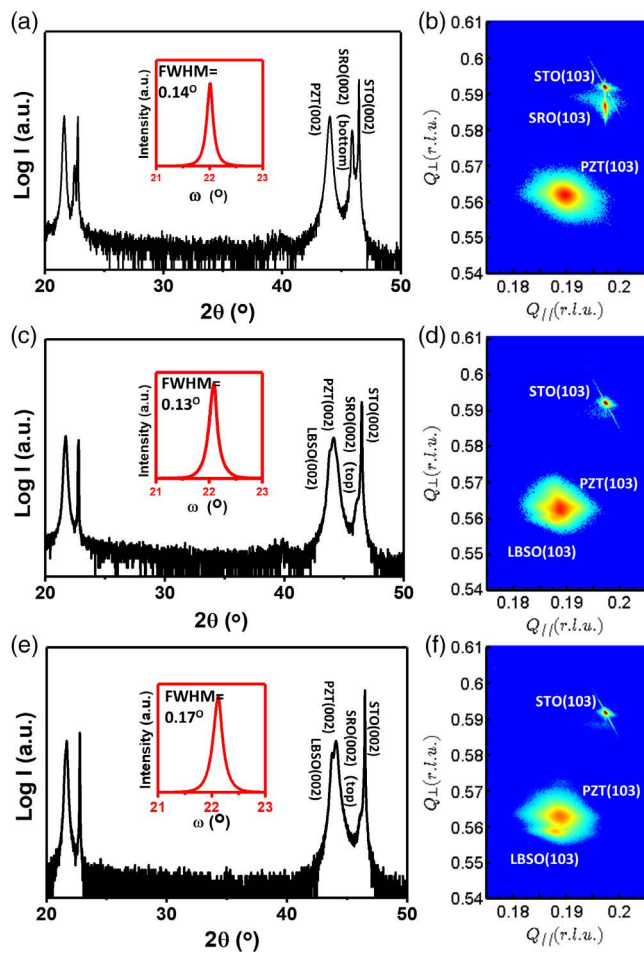
ADVANCED
SCIENCE NEWS
www.advancedsciencenews.com

pss rrl
physica status solidi
www.pss-rapid.com

Figure 2. XRD 001 measurement of a) SRO/PZT/SRO, c) SRO/PZT/LBSO, and e) SRO/PZT/2 nm SRO/LBSO thin films on STO substrates and the reciprocal maps around the (103) peaks of b) SRO/PZT/SRO, d) SRO/PZT/LBSO, and f) SRO/PZT/2 nm SRO/LBSO thin films on STO substrates.

The PZT thin film in the latter device has an in-plane lattice constant $a_m = 4.080$ Å and an out-of-plane lattice constant $c_m = 4.104$ Å ($c_m/a_m = 1.006$), equal to those of the SRO/PZT/LBSO device. This indicates that the average strain state of the PZT in both devices is the same and that the 2 nm SRO layer is fully epitaxially strained to the LBSO, as is also evidenced by the SRO/LBSO interface in STEM (see Figure S1, Supporting Information). We note that the mentioned lattice parameters are domain fraction averaged over, respectively, the in-plane and out-of-plane lattice parameters in the nanosized c and a domains.[37] In the bulk of the PZT film, the domain fraction adapts to obtain zero stress and with that a lowest energy state in the film.[38] Both capacitor structures are subjected to the same thermal strain arising from the difference in thermal expansion coefficients of substrate and PZT. Therefore, in principle, the domain fractions and with that the average lattice parameters should be the same in all three devices. The slight differences in measured average lattice parameters are attributed to differences in the thickness of the initial growth layer of PZT. In general, in the case of perfect epitaxy, the thickness of a strain relaxation layer, d, at an interface of two materials with different in-plane lattice parameters scales with the interdislocation distance at the interface, $1/\rho$, which can be expressed in terms of the substrate lattice parameter a_s, and the effective lattice mismatch ε_m^* (that takes a value between 0 and $\varepsilon_m = (a_s - a)/a$), as $d = 1/\rho = a_s/\varepsilon_m^*$.[20,39] This shows that the strain gradient layer thickness increases with decreasing lattice mismatch. One can interpret this result also such that with increasing (dislocation) defect density, the strain relaxation is easier, and consequently, the strain relaxation layer becomes thinner. We think that at the PZT/SRO bottom interface most epitaxial strain is relaxed by a relatively high density of dislocation defects, needed to accommodate the large (effective) lattice mismatch, within a few nanometers of the PZT, whereas the small lattice mismatch at the PZT/(2 nm SRO)/LBSO interface causes a relatively thick strain relaxation layer with a lower dislocation density at this interface. (We note that the transmission electron microscopy [TEM] analysis does not show any other defects than dislocation defects at interfaces; therefore, we think that lattice dislocations form the main mechanism for strain relaxation.) Such changes in strain relaxation layer thickness have been observed from XRD analysis on a series of 25 nm thick PZT layers with different Ti contents, and therefore with different lattice parameters, thus with different lattice mismatch with the SRO/STO substrate.[40]

Atomic force microscopy (AFM) images of the surfaces of SRO and LBSO bottom electrodes are shown in **Figure 3**a,b, respectively. The insets give corresponding cross-sectional profiles. In Figure 3a, the step-terrace structure is clearly observed, indicating coherent growth and a very smooth surface. Peak-to-peak height differences are about 0.4 nm. Although the LBSO thin film is not atomically smooth and the imprint of the substrate step-terrace structure is absent, the LBSO is still very smooth, and the peak-to-peak height difference is less than 0.5 nm (Figure 3b). Again, we attribute these differences in surface morphology to the large lattice mismatch between LBSO and STO as compared with the full epitaxially strained growth of SRO on STO. The chemically sharp interface between PZT and LBSO, as shown by EELS–STEM (Figure 1), and the smooth surface of the bottom electrodes, as shown by AFM, suggest that chemical effects and surface roughness effects can be ruled out in these systems.

From the structural measurements, we conclude that the main difference between PZT grown on LBSO/STO and on SRO/STO is the rapid strain relaxation by a relatively high dislocation density in the first few unit cells of PZT in the latter case, whereas in the cases of LBSO/STO and 2 nm SRO/LBSO/STO, the dislocation density is low and the strain relaxation extends over a larger thickness (of the order of 10 nm).

The polarization hysteresis (P–E) loops of SRO/PZT/SRO, SRO/PZT/LBSO, and SRO/PZT/2 nm SRO/LBSO capacitors, measured at 1 kHz, are shown in **Figure 4**a. The typical ferroelectric behavior is clearly present for all three systems. They show a similar saturation polarization value P_s of about 40 μC cm^{-2}. The measured positive and negative remanent polarization (P_{rm}^+ and P_{rm}^-) and measured coercive field (E_{cm}^+ and E_{cm}^-) values are shown in **Table 1** (index m for measured). The (measured) average coercive field of the SRO/PZT/LBSO device (72.0 kV cm^{-1}), calculated as $E_{cm} = (E_{cm}^+ - E_{cm}^-)/2$, is larger than that of the SRO/PZT/SRO device (48.2 kV cm^{-1}). The 2 nm SRO layer,
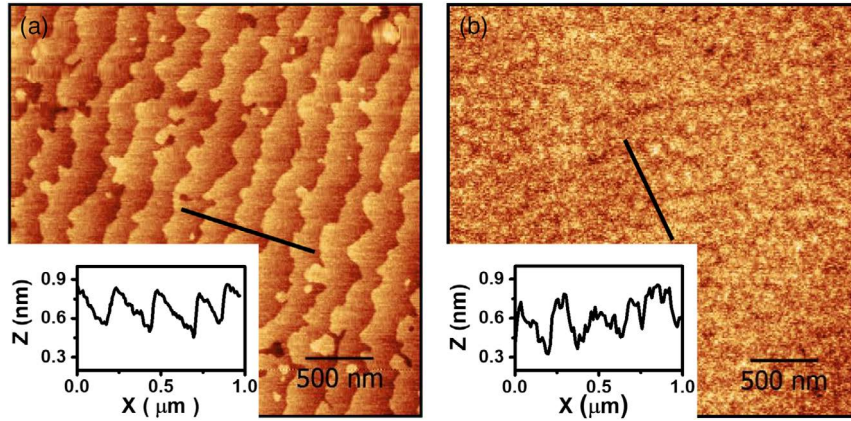
**ADVANCED
SCIENCE NEWS**

www.advancedsciencenews.com

pss rrl

physica status solidi

www.pss-rapid.com

Figure 3. AFM images of bottom electrodes a) SRO thin film and b) LBSO thin film on STO substrates.
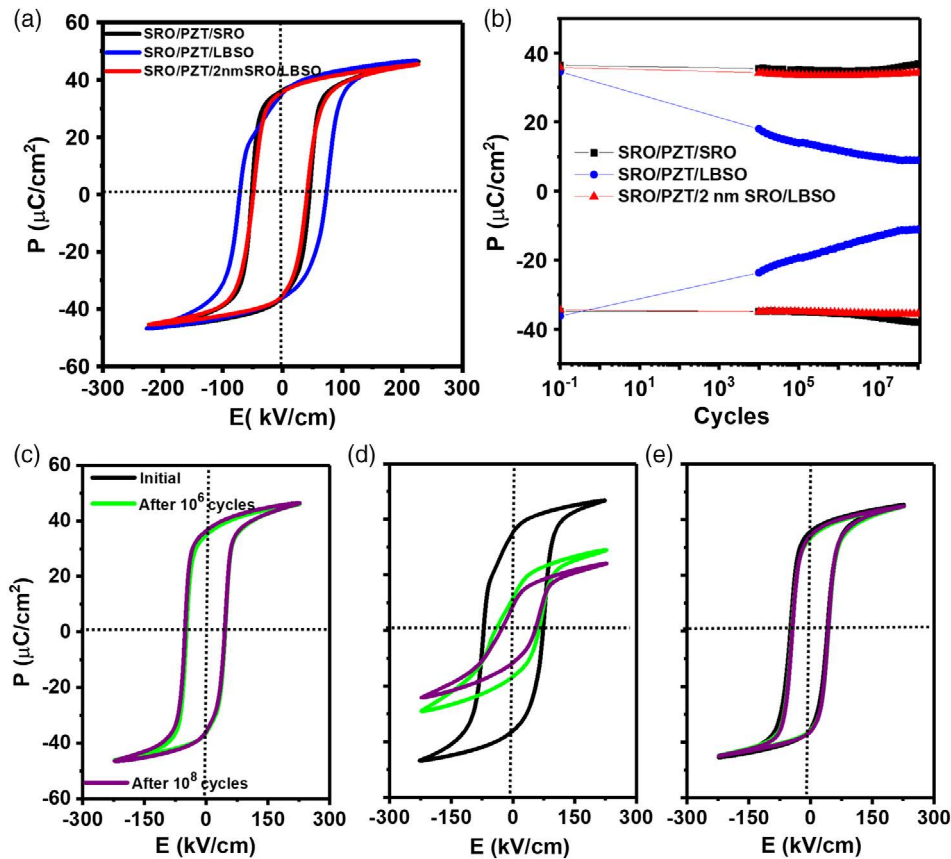

Figure 4. a) Initial P–E loops of the PZT thin film in SRO/PZT/SRO, SRO/PZT/LBSO, and SRO/PZT/2 nm SRO/LBSO capacitors. b) Remanent polarization during fatigue measurement for three devices performed under bipolar switching pulse of 160 kV cm^{-1} and frequency of 100 kHz. P–E loops at initial, after 10^6, and after 10^8 switching cycles for the c) SRO/PZT/SRO, d) SRO/PZT/LBSO, and e) SRO/PZT/2 nm SRO/LBSO capacitors.

inserted between the PZT and the bottom electrode LBSO, reduces the average coercive field to a value similar to that of the SRO/PZT/SRO device. In first instance, it may be somewhat surprising that the (measured) imprint or self-bias fields, calculated as $E_{sbm} \equiv (E_{cm}^+ + E_{cm}^-)/2$, are both fairly small (only a few kilovolts per centimeter) for the symmetric (SRO/PZT/SRO) and asymmetric (SRO/PZT/LBSO) devices, as it is regularly stated in the literature that different electrodes give rise to imprint due to different work function values.

When a positive voltage is applied to the top electrode, coming from negative poling, the polarization is more likely to point away from the top electrode, and reverse domain nucleation is likely to occur at the interface between PZT and the top electrode. We, therefore, assume that the positive coercive field corresponds

ADVANCED
SCIENCE NEWS
www.advancedsciencenews.com

pssrrl
physica status solidi
www.pss-rapid.com

Table 1. Positive and negative remnant polarizations, measured coercive fields, calculated intrinsic coercive field, and net intrinsic self-bias field values for the three capacitors.

	SRO/PZT/SRO	SRO/PZT/LBSO	SRO/PZT/2 nm SRO/LBSO
		Initial (after 10^8 cycles)	
P_r^+ [µC cm^{-2}]	36.3	34.6 (9.4)	35.9
P_r^- [µC cm^{-2}]	−34.8	−36.2 (−11.8)	−34.4
E_{cm}^+ [kV cm^{-1}]	45.9	72.5 (52.8)	40.8
E_{cm}^- [kV cm^{-1}]	−50.5	−71.5 (−29.9)	−48.9
E_{cm} [kV cm^{-1}]	48.2	72.0 (41.4)	44.9
E_{sbm} [kV cm^{-1}]	−2.3	0.5 (11.5)	−4
E_{ci}^+ [kV cm^{-1}]	48.2	48.2 (48.2)	48.2
E_{ci}^- [kV cm^{-1}]	−48.2	−95.8 (−34.5)	−41.5
E_{sbi} [kV cm^{-1}]	2.3	−24.3 (−4.6)	7.4

to reverse domain nucleation at the top interface. Analogously, the negative coercive field corresponds to reverse domain nucleation at the interface between the PZT and the bottom electrode.[41]

The intrinsic coercive fields E_{ci}^+ and E_{ci}^- at the PZT–electrode interfaces (index i for intrinsic), which are the values of a locally applied electrical field to create reverse domain nucleation at that interface, can therefore be written as

$$E_{ci}^+ = E_{cm}^+ + E_{sbi} \tag{1}$$

$$E_{ci}^- = E_{cm}^- + E_{sbi} \tag{2}$$

E_{sbi} is a net intrinsic self-bias field present in the system, which can be very different from the "measured" value E_{sbm}. The first has a physical basis within the device, whereas the latter is the effective manifestation in the polarization hysteresis loop. In the SRO/PZT/SRO capacitor, the interfaces at both sides are between SRO and PZT. We expect that in this case, the values of positive and negative intrinsic coercive fields E_{ci}^+ and E_{ci}^- can be assumed to be the same. The intrinsic coercive field of the PZT–SRO interface $E_{ci-SRO}^+ = -E_{ci-SRO}^-$ is then obtained as 48.2 kV cm^{-1} (see Table 1) and the net intrinsic self-bias field as 2.3 kV cm^{-1}. In the SRO/PZT/LBSO capacitor, the above-deduced intrinsic coercive field of the PZT/SRO interface E_{ci-SRO}^+ can be used for the intrinsic coercive field of the top interface. The intrinsic coercive field of the PZT/LBSO interface at negative side $E_{ci-LBSO}^-$ is then derived as −95.8 kV cm^{-1} from Equation (2). The large difference with the coercive field of the PZT/SRO interface hints toward a significant difference in the properties of the LBSO/PZT and SRO/PZT interfaces. In the model of interface-stimulated nucleation of reverse domains,[39] the interfacial energy per unit area of the interface of the reverse domain with the electrode, $\gamma = \zeta P_s$, determines largely the coercive field value. In this expression, ζ is the surface analogon of the field, E, for the free energy per unit volume EP_s and P_s the saturation polarization in the reversal domain. Furthermore, we show that there is a static field at the LBSO/PZT interface that varies strongly with field cycling. We think that this field may determine the value of ζ and is the reason

behind the large value of $E_{ci-LBSO}^-$ as compared with E_{ci-SRO}^+. In addition, the different strain state of the initial growth layer of PZT on LBSO as compared with PZT on SRO, due to the different defect densities, may play a role in the reverse domain nucleation. Although this cannot explain the change of the coercive field with cycling, as it is not expected that cycling changes the strain, it may be the reason for the large initial coercive field at the PZT/LBSO interface. The intrinsic self-bias field in this asymmetric device is calculated as −24.3 kV cm^{-1}. The very small measured self-bias, E_{sbm}, of the nearly symmetric P–E loop shown in Figure 4a for this asymmetric system seems therefore coincidental and caused by the large difference in intrinsic coercive fields and the large net intrinsic self-bias field. By introducing the 2 nm SRO layer in between the PZT and the LBSO, the coercive field of this interface is nearly fully restored to that of the top SRO/PZT interface, again demonstrating the large difference in interface properties for the different electrode materials. In addition, the intrinsic self-bias field has nearly fully returned to the values of the SRO/PZT/SRO device.

Figure 4b shows the polarization as a function of the number of switching cycles for the three different devices. As in a previous work by Nguyen,[13] it shows that SRO/PZT/SRO is highly resistant to fatigue up to at least 10^8 switching cycles. However, the remanent polarization decreases approximately logarithmically with cycle number for the PZT on the LBSO bottom electrode. This fatigue behavior is completely suppressed by adding the 2 nm SRO layer between PZT and LBSO. This again shows the difference in interfacial properties between the LBSO/PZT and the SRO/PZT interfaces. The P–E loops at different fatigue stages, the initial loop and after 10^6 and 10^8 cycles, for the SRO/PZT/SRO, SRO/PZT/LBSO, and SRO/PZT/2 nm SRO/LBSO devices are shown in Figure 4c–e, respectively. For the SRO/PZT/LBSO capacitor (Figure 4d), the loops become more asymmetric after many switching cycles (green and purple lines in Figure 4d). Based on Equation (1) and (2), the intrinsic coercive field of the PZT–LBSO interface decreases from −95.8 kV cm^{-1} in the initial stage to −34.5 kV cm^{-1} after 10^8 switching cycles. The net intrinsic self-bias field in PZT also changes from −24.3 kV cm^{-1} in the initial stage to −4.6 kV cm^{-1} after 10^8 switching cycles (see Figure S2, Supporting Information). In the following sections, we discuss a plausible physical mechanism that explains this fatigue behavior as well as the change in coercive field and self-bias field with cycling. Finally, we noted a "sloped" section in the second quadrant of the P–E loop, which is not discussed further here.

Figure 5a–c shows the capacitance–voltage (C–V) measurements for the various devices in the initial stage and after 10^6 switching cycles with the characteristic anticlockwise butterfly loops. The peaks are associated with the polarization reversal. In the SRO/PZT/SRO device (Figure 5a), the initial capacitance is equal for both high field polarities. The C–V curve after 10^6 switching cycles is the same as the initial curve, reflecting the stability against field cycling. In the SRO/PZT/LBSO device, the initial capacitance is ≈0.180 nF at −340 kV cm^{-1} and ≈0.185 nF at 340 kV cm^{-1}. The capacitance difference for both high field side polarities indicates the imperfect screening at the PZT/LBSO interface. We think that this is a consequence of the fact that LBSO is a metal with a very low free electron density (when compared with SRO). At a positive voltage, the
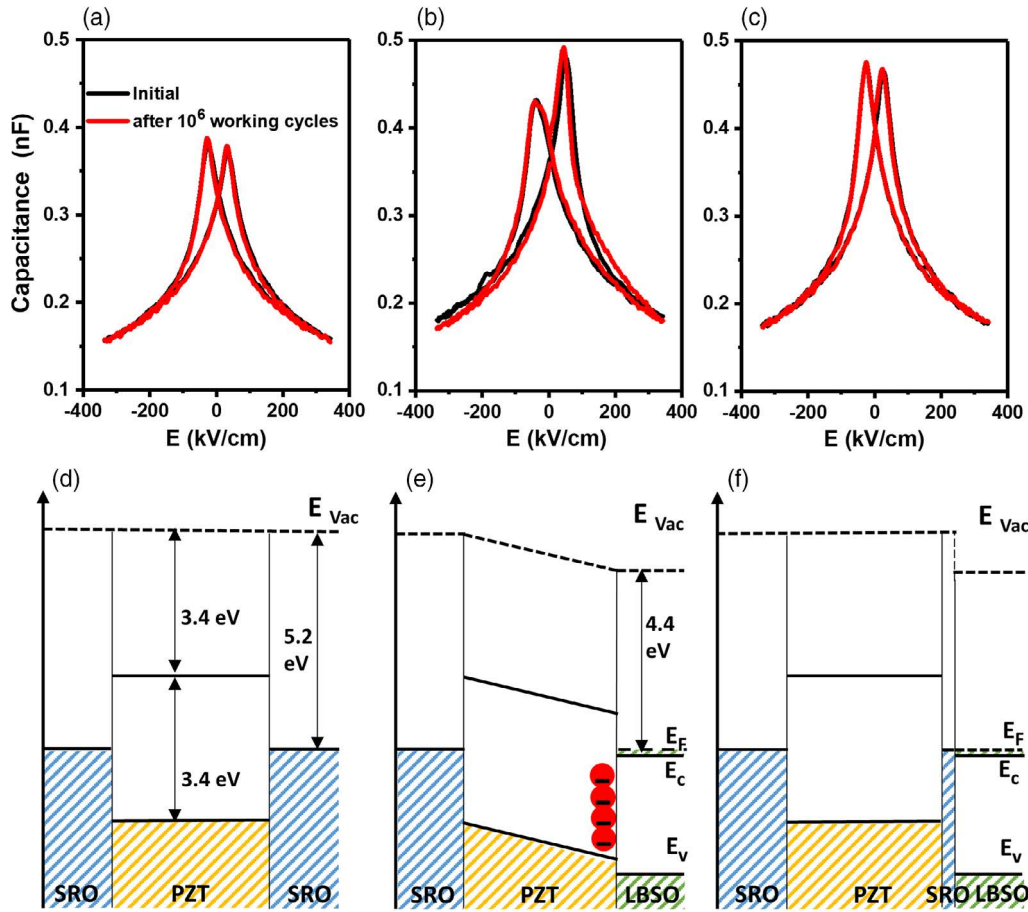
**ADVANCED
SCIENCE NEWS**

www.advancedsciencenews.com

pss rrl
physica status solidi

www.pss-rapid.com

Figure 5. Capacitance–voltage (C–V) curves of a) SRO/PZT/SRO, b) SRO/PZT/LBSO, and c) SRO/PZT/2 nm SRO/LBSO capacitors at the initial stage and after 10^6 switching cycles. Schematic band diagrams of d) SRO/PZT/SRO, e) SRO/PZT/LBSO, and (f) SRO/PZT/2 nm SRO/LBSO heterostructure.

polarization points toward the bottom electrode creating a positive polarization charge at the LBSO/PZT interface and a negative screening charge in the electrode. In this case, the screening layer thickness is negligible. In the case of negative bias on the top electrode, the positive charge in the bottom electrode, screening the negative polarization charge, extends over a finite screening length into the LBSO electrode. Assuming that for positive bias the interfacial capacitance is negligible, then in this case the total capacitance C_{tot}^+ is determined by the capacitance of the PZT layer only: $C_{tot}^+ = C_{PZT}$. For negative voltage, the total capacitance C_{tot}^- is then given by $1/C_{tot}^- = 1/C_{PZT} + 1/C_D$, where C_D is the interfacial capacitance. By combining these relations, we obtain

$$C_D = \frac{1}{1/C_{tot}^- - 1/C_{PZT}} = \varepsilon_0 \varepsilon_d A/d \qquad (3)$$

The thickness of the screening layer d at the LBSO/PZT interface is about 1.06 nm assuming a dielectric constant of BaSnO₃ (BSO) $\varepsilon_d = 20$ and a capacitor area $A = 4 \times 10^{-8}$ m².[29] This agrees well with the Thomas–Fermi screening length $r_{LBSO} = \frac{1}{2}\left(\frac{a_0^3}{n}\right)^{1/6} = 0.95$ nm, where the Bohr radius $a_0 = \left(\frac{0.53\varepsilon}{m_e/m_0}\right)$ Å = 26.5 Å is that of BSO for $\varepsilon_d = 20$, effective mass

$m_e = 0.4\,m_0$, and carrier density $n = 4 \times 10^{20}$ cm⁻³.[29] The screening length of SRO is only 0.07 nm due to the high carrier density of 2×10^{22} cm⁻³. This explains the difference in C–V loops of the SRO/PZT/SRO and SRO/PZT/LBSO capacitors (Figure 1a,b). After 10^6 switching cycles, the SRO/PZT/LBSO capacitance at -340 kV cm⁻¹ reduces slightly to 0.170 nF and at 340 kV cm⁻¹ to 0.180 nF (Figure 5b), indicating the formation of an additional (interfacial) capacitance layer in series with the PZT capacitance.[42] This result implies that any interfacial capacitance that might already have been present in the initial state has changed due to cycling. In the following, we will argue that this is due to electron injection from the LBSO into the PZT upon cycling.

Interestingly, the introduced 2 nm SRO intermediate layer is able to suppress the formation of a finite-thickness depletion layer, because of the high electron density of SRO. As shown in Figure 5c, the C–V curve after 10^6 cycles remains the same as that at the initial stage, indicating that the effect of the interfacial capacitance is negligible.

Figure 5d–f shows schematically simplified band diagrams of the various capacitors using the data in Table S1, Supporting Information. We assume that the free electron density in PZT is so low that the screening length is large compared with the

film thickness, so the potential drop in the PZT can be assumed to be linear. (The argument that the electron density is low is supported by the very low leakage current measured in our devices.) Here, the electrodes are considered to be ideal metals. Further, we neglect for simplicity the presence of interface dipoles.[43]

The 0.8 eV difference in work functions, $\Delta W = W_{LBSO} - W_{SRO}$, between the SRO and LBSO electrodes results in the slope in the band edges that can be translated into an intrinsic self-bias field $E^-_{sbi-LBSO} = (W_{LBSO} - W_{SRO})/d_{PZT} = -18.2$ kV cm^{-1}, directed from the bottom to the top electrode. (d_{PZT} is the thickness of the PZT layer). This agrees in sign and fairly well in value with the intrinsic self-bias field of -24.3 kV cm^{-1} determined from the $P–E$ loop of the SRO/PZT/LBSO device. (Vice versa the deduced $E_{sbi} = -24.3$ kV cm^{-1} would translate into a work function difference of 1.1 eV. This would correspond to an even lower LBSO/PZT interfacial barrier height of 0.7 eV.)

Inserting the 2 nm SRO layer reduces the self-bias field again significantly to a value that corresponds to an effective work function difference $W_{top} - W_{bot} = 0.3$ eV (calculated from the determined E_{sbi} value), which is close to that measured for the symmetric device (0.1 eV). This indeed suggests that the effective work function at the bottom PZT/2 nm SRO/LBSO interface is nearly that of SRO. The small discrepancies might be due to uncertainties in the work function values and/or the effect of Fermi level pinning at the interface by defects.

The fatigue cycling changes the properties of the LBSO/PZT interface. We explain this in terms of the electron injection model described in the literature.[12,44] During switching, reverse domains are nucleating at the interface, leading to an extremely large temporary local electrical field in the reversal domains of the value $E_{loc} \sim P_s/\varepsilon_0\varepsilon_i$, where ε_i is the dielectric constant of a low-dielectric-constant layer at the electrode/PZT interface.[12,44] (The Supporting Information explains in more detail the different macroscopic and local fields in and around the reverse domain.) Electrons are injected from the electrode into the ferroelectric by this local field. Defect states, introduced during the growth (we think these are mainly oxygen vacancies, but also the dislocation defects), can trap these injected electrons near the interfaces. The finite screening length of the LBSO creates an insulating, low-dielectric-constant layer that enhances strongly the local field at the PZT/LBSO arising during switching. In the Fowler–Nordheim model, the tunnel/injection current $J = C_{FN}E^2_{loc}\exp\left[-\frac{8\pi\sqrt{2m_e}(q\Phi_B)^{3/2}}{3qE_{loc}}\right]$, where $C_{FN} = \frac{q^2}{8\pi h \Phi_B}$. The symmetric SRO/PZT/SRO device has high interfacial barrier potentials of $\Phi_B = 1.8$ eV, preventing easy charge injection into possible gap states in the PZT. For the LBSO/PZT interface, this barrier is much lower (1.0 eV); thus charge injection to trap states is much more likely to take place. Even more significantly, the PZT/SRO interfaces do not show a low-dielectric-constant layer, whereas in the LBSO/PZT interfaces such a layer arises due to the depletion of the LBSO conduction band over a width equal to the screening length.[45]

In drawing the band diagram of the SRO/PZT/2 nm SRO/LBSO device, we have assumed that the full SRO/PZT barrier height is restored by the insertion of the 2 nm SRO layer, which would imply that the charge injection chance is reduced again

significantly. A 2 nm thick SRO would in principle be able to supply 4×10^{15} electrons cm^{-2} to screen a polarization charge density of 2.3×10^{14} electrons cm^{-2}. Even if a large fraction of the SRO thickness is not participating in the screening (a "dead" interfacial layer), full screening is likely to be possible if at least a layer with a thickness larger than the Thomas–Fermi screening length (0.07 nm) has bulk properties. This layer can provide sufficient conduction electron states not to become completely depleted or filled by the screening. (Note that additional electrons can always be supplied by the connected LBSO reservoir.) We think that this is a sufficient condition so that the SRO layer can restore the band alignment to that of the bulk SRO/PZT interface. Second, when the 2 nm SRO layer is inserted the low-dielectric-constant layer, which enhances the local field, in LBSO is not present anymore. As the local electrical field induced by reversal domains is larger (and the interfacial barrier much lower) at the LBSO/PZT interface than at the SRO/PZT interface, we expect that electron injection and subsequent trapping is much more likely to happen at the LBSO/PZT interface (noted in Figure 5e). Thus, with the number of switching cycles, the amount of trapped charge (per unit area), σ_{tr}, increases and creates an electric field E_σ directed from the top electrode to the bottom electrode in the PZT (opposite to the self-bias field induced by the work function difference). This increasing electric field E_σ can ultimately pin the polarization, causing the observed fatigue. We note that the injection current scales approximately linearly with the density of available trap sites, which in turn is likely to scale with the defect density. Thus, one might expect a higher injection probability for the SRO/PZT interface, for which we have assumed a high defect density, as compared with the LBSO/(2 nm SRO)/PZT interface. This trap density dependence of the injection probability is however outweighed by the exponential dependence on interfacial barrier height and dielectric constant.

The injected charge changes the self-bias field in the areas that are still switchable and thus observable in the fatigue hysteresis loop, as well as in the nonswitchable areas. For the switchable fraction of the polarization in the fatigued SRO/PZT/LBSO device, the self-bias field can be estimated from the $P–E$ loops (Figure 4d), using Equation (1) and (2) as $E^{fat}_{sbi} = -4.6$ kV cm^{-1}. This field is the net effect of the intrinsic self-bias field of the initial stage, E^{in}_{sbi}, and the electric field arising from the trapped electrons in the switchable areas, E^{sw}_σ

$$E^{fat}_{sbi} = E^{in}_{sbi} + E^{sw}_\sigma \qquad (4)$$

From this, one can estimate $E^{sw}_\sigma = 19.7$ kV cm^{-1} (after 10^8 cycles), directed from the top to the bottom electrode. Using Gauss's law $E^{sw}_\sigma = \sigma_{sw}/2\varepsilon_0 = n_{tr}e/2\varepsilon_0$ the trapped electron charge density, n_{tr}, is estimated as 2.2×10^{10} cm^{-2} (or 3.6×10^{-5} electron per unit cell area, or 3.5×10^{-5} C m^{-2}). If one assumes that the field created by trapped charge causes the polarization to be nonswitchable in the nonswitchable areas of the capacitor, then the trapped charge density, σ_{nonsw}, is much larger. In that case E^{nonsw}_σ has to be larger than at least the maximum applied field plus the measured coercive field (≈ 300 kV cm^{-1}), and the associated minimum trapped charge density is estimated as $\sigma_{nonsw} \approx 3.3 \times 10^{11}$ cm^{-2} (or 5.4×10^{-4} electron per unit cell area). The change in the depletion layer at the PZT/LBSO

ADVANCED SCIENCE NEWS
www.advancedsciencenews.com

pss rrl
physica status solidi
www.pss-rapid.com

interface, as indicated by the C–V measurement (Figure 5b), is expected to be caused by the charge injection. An alternative mechanism may be that a high σ_{nonsw} value pins the domain walls and in that way prevents switching.

To further substantiate the electron injection and trapping model, the fatigued device SRO/PZT/ LBSO was illuminated with white light for 1.5 h or alternatively stored in the dark for 1.5 h. Figure S3, Supporting Information, shows that the remnant polarization increases significantly after illumination, but the polarization does not recover for the fatigued device placed in the dark. This indicates that the trapped electrons in the PZT are removed by the light, leading to the polarization recovery. This result also supports the charge injection and trapping model.

In conclusion, PZT thin films with excellent crystalline quality and chemical sharp interfaces of the bottom LBSO, respectively SRO electrode with a ferroelectric PZT layer were obtained. Differences in strain and thickness of the strain relaxation layer at the PZT/bottom electrode interface relate to the differences in dislocation density, which in turn arise from the differences in lattice mismatch between PZT and electrode materials.

In contrast to a PZT-on-SRO electrode device, a large coercive field and strong fatigue behavior are observed for PZT with a LBSO bottom electrode. The observed fatigue behavior is explained by charge injection and trapping at the PZT/LBSO interface into the ferroelectric layer up to a depth corresponding to the size of the reverse domain.

Ultimately, the electric field induced by injected charge leads to polarization fatigue. The fatigue can be remedied by introducing an only 2 nm thick SRO layer between PZT and LBSO. It is argued that the introduced SRO layer suppresses the charge injection, because of its large carrier density as compared with LBSO, and the large interfacial barrier with PZT.

This work clearly shows that the work function and carrier density of oxide electrodes in ferroelectric devices play an important role in the polarization switching and fatigue properties of the ferroelectric layer.

Experimental Section

Sample Fabrication: The PLD growth conditions were optimized with respect to surface morphology, crystalline quality, and functional properties. For the LBSO growth, the background oxygen pressure was set at 0.13 mbar and the substrate temperature at 830 °C. Laser ablation was performed with a fluence of 1.3 J cm^{-2}, a frequency of 1 Hz, and a spot size of 0.59 mm^2. PZT was grown at an oxygen pressure of 0.1 mbar, a substrate temperature of 600 °C, a laser fluence of 2 J cm^{-2}, and a laser frequency of 10 Hz. SRO was grown at an oxygen pressure of 0.25 mbar, a substrate temperature of 600 °C, and the laser fluence and frequency were 2 J cm^{-2} and 4 Hz, respectively. A spot size of 2.3 mm^2 was used for both SRO and PZT. The thickness of the SRO and LBSO layers was ≈50 nm and that of the PZT layer was 440 nm for all capacitors. To measure the electrical properties, capacitor structures were patterned by photolithography and ion beam dry etching.

Sample Characterization: The structural and chemical properties of the interfaces between the electrodes and PZT were visualized by Cs-corrected scanning transmission electron microscopy (STEM), equipped with a Gatan Enfina spectrometer for EELS. The microscope was operated at 300 kV with a 20 mrad convergence angle. Crystallographic properties of the thin films were investigated by XRD (Panalytical MRD). Surface morphology was investigated by AFM (Bruker). The out-of-plane polarization

hysteresis loop (P–E) was measured with the aixACCT TF2000. The applied field range was −225 to 225 kV cm^{-1}. Fatigue measurements were performed using bipolar rectangular field pulses of 160 kV cm^{-1} with a repetition frequency of 100 kHz. The capacitance of the PZT heterostructure reflects the interaction of free carriers at the interface between PZT and the electrodes. A slowly scanning direct current (DC) bias voltage in the range from −340 to 340 kV cm^{-1} and a low-field (1.1 kV$_{pp}$ cm^{-1}) alternate current (AC) modulation with a frequency of 100 kHz were applied to measure the field dependence of the (AC) capacitance across the heterostructure. In all electrical experiments, the bottom electrode was grounded.

Conflict of Interest

The authors declare no conflict of interest.

[1] *Physics of Ferroelectrics: A Modern Perspective*, 1st ed. (Eds: K. M. Rabe, C. H. Ahn, J.-M. Triscone), Springer-Verlag, Berlin, Heidelberg **2007**.

[2] T. Choi, S. Lee, Y. Choi, V. Kiryukhin, S.-W. Cheong, *Science* **2009**, *324*, 63.

[3] D. S. Jeong, R. Thomas, R. Katiyar, J. Scott, H. Kohlstedt, A. Petraru, C. S. Hwang, *Rep. Prog. Phys.* **2012**, *75*, 076502.

[4] Y. Nishitani, Y. Kaneko, M. Ueda, E. Fujii, A. Tsujimura, *Jpn. J. Appl. Phys.* **2013**, *52*, 4S.

[5] V. Garcia, M. Bibes, *Nat. Commun.* **2014**, *5*, 4289.

[6] A. Ghosh, G. Koster, G. Rijnders, *Adv. Funct. Mater.* **2016**, *26*, 5748.

[7] J. Junquera, P. Ghosez, *Nature* **2003**, *422*, 506.

[8] J. F. Scott, C. A. P. De Araujo, *Science* **1989**, *246*, 1400.

[9] O. Auciello, J. F. Scott, R. Ramesh, *Phys. Today* **1998**, *51*, 22.

[10] C. Ahn, J.-M. Triscone, J. Mannhart, *Nature* **2003**, *424*, 1015.

[11] V. Nagarajan, I. Jenkins, S. Alpay, H. Li, S. Aggarwal, L. Salamanca-Riba, A. Roytburd, R. Ramesh, *J. Appl. Phys.* **1999**, *86*, 595.

[12] X. Lou, M. Zhang, S. Redfern, J. Scott, *Phys. Rev. Lett.* **2006**, *97*, 177601.

[13] M. D. Nguyen, *Ph.D. Thesis*, University of Twente, **2010**.

[14] M. Dawber, K. Rabe, J. Scott, *Rev. Mod. Phys.* **2005**, *77*, 1083.

[15] G. Rijnders, D. H. Blank, *Nature* **2005**, *433*, 369.

[16] M.-S. Chen, T.-B. Wu, J.-M. Wu, *Appl. Phys. Lett.* **1996**, *68*, 1430.

[17] H. T. Vu, M. D. Nguyen, E. Houwman, M. Boota, M. Dekkers, H. N. Vu, G. Rijnders, *Mater. Res. Bull.* **2015**, *72*, 160.

[18] J. Lee, C. Thio, S. B. Desu, *J. Appl. Phys.* **1995**, *78*, 5073.

[19] A. K. Tagantsev, I. Stolichnov, E. Colla, N. Setter, *J. Appl. Phys.* **2001**, *90*, 1387.

[20] A. Tagantsev, G. Gerra, *J. Appl. Phys.* **2006**, *100*, 051607.

[21] L. Pintilie, M. Alexe, *J. Appl. Phys.* **2005**, *98*, 124103.

[22] G. Le Rhun, G. Poullain, R. Bouregba, *J. Appl. Phys.* **2004**, *96*, 3876.

[23] H. Paik, Z. Chen, E. Lochocki, A. Seidner H, A. Verma, N. Tanen, J. Park, M. Uchida, S. Shang, B.-C. Zhou, M. Brützam, R. Uecker, Z.-K. Liu, D. Jena, K. M. Shen, D. A. Muller, D. G. Schlom, *APL Mater.* **2017**, *5*, 116107.

[24] H. J. Kim, U. Kim, H. M. Kim, T. H. Kim, H. S. Mun, B.-G. Jeon, K. T. Hong, W.-J. Lee, C. Ju, K. H. Kim, K. Char, *Appl. Phys. Express* **2012**, *5*, 061102.

[25] B. Noheda, J. Gonzalo, L. Cross, R. Guo, S.-E. Park, D. Cox, G. Shirane, *Phys. Rev. B* **2000**, *61*, 8687.

[26] F. Chen, H. Wang, Q. Liu, W. Wu, X.-G. Li, *Appl. Phys. Lett.* **2007**, *90*, 082904.

[27] S. Alpay, I. Misirlioglu, V. Nagarajan, R. Ramesh, *Appl. Phys. Lett.* **2004**, *85*, 2044.

[28] H.-R. Liu, J.-H. Yang, H. Xiang, X. Gong, S.-H. Wei, *Appl. Phys. Lett.* **2013**, *102*, 112109.

[29] H. J. Kim, U. Kim, T. H. Kim, J. Kim, H. M. Kim, B.-G. Jeon, W.-J. Lee, H. S. Mun, K. T. Hong, J. Yu, K. Char, K. H. Kim, *Phys. Rev. B* **2012**, *86*, 165205.

[30] S. A. Chambers, T. C. Kaspar, A. Prakash, G. Haugstad, B. Jalan, *Appl. Phys. Lett.* **2016**, *108*, 152104.

[31] H. Yang, H. Luo, H. Wang, I. Usov, N. Suvorova, M. Jain, D. Feldmann, P. Dowden, R. DePaula, Q. Jia, *Appl. Phys. Lett.* **2008**, *92*, 102113.

[32] Y. Hikita, Y. Kozuka, T. Susaki, H. Takagi, H. Hwang, *Appl. Phys. Lett.* **2007**, *90*, 143507.

[33] W. Siemons, G. Koster, A. Vailionis, H. Yamamoto, D. H. Blank, M. R. Beasley, *Phys. Rev. B* **2007**, *76*, 075126.

[34] G. Koster, B. L. Kropman, G. J. Rijnders, D. H. Blank, H. Rogalla, *Appl. Phys. Lett.* **1998**, *73*, 2920.

[35] I. Vrejoiu, G. Le Rhun, L. Pintilie, D. Hesse, M. Alexe, U. Gösele, *Adv. Mater.* **2006**, *18*, 1657.

[36] X.-K. Wei, Y. Yang, L. J. McGilly, L. Feigl, R. E. Dunin-Borkowski, C.-L. Jia, L. Bellaiche, N. Setter, *Phys. Rev. B* **2018**, *98*, 020102.

[37] R. J. A. Steenwelle, *Ph.D. Thesis*, University of Twente, **2012**.

[38] E. P. Houwman, K. Vergeer, G. Koster, G. Rijnders, *Correlated Functional Oxides* Springer, Cham, Switzerland, **2017**, p. 29.

[39] G. Gerra, A. Tagantsev, N. Setter, *Phys. Rev. Lett.* **2005**, *94*, 107602.

[40] M. Boota, E.P. Houwman, M. Dekkers, *Appl. Phys. Lett.* **2014**, *104*, 182909.

[41] This is a possible consequence of the explanation given by Tagantsev and Gerra in their review paper on interface effects[20] for the strong reduction of the coercive field by orders of magnitude, by interface-stimulated nucleation of reverse domains, due to the contribution of interfacial energy, $\gamma = \zeta P_s$ of the nucleating reversal domain with the electrode to the total energy of the nucleus. Here, ζ is considered as the surface equivalent of the electric field. Considering $\gamma = \zeta P_s$ as a vector product (in analogy with the volume energy term **EP**), then the direction of the polarization becomes very important. For negative γ, the coercive field even increases above the value for $\gamma = 0$! Consequently, in practice reverse nucleation domains arise first (when changing applied field) when the ζ vector and polarization have the same direction ($\gamma > 0$) and at only one electrode. In assuming that the positive (respectively, negative) coercive field corresponds to reverse domain nucleation at the top (bottom) interface, we have—within the framework of this nucleation model—implicitly assumed that the ζ vector is pointing into the ferroelectric at both interfaces (which corresponds with the explanatory figure [Figure 14] given in ref. [20]). Further experimental investigation is required that this is indeed the case.

[42] The capacitance change is approximately constant in the range -340 to -200 kV cm^{-1} (respectively, 200–340 kV cm^{-1}). was calculated from the extreme field values, but could have been calculated at any field value in this range.

[43] In discussion with the reviewers we realized this is a strong simplification of the physics. In the Supporting Information we reconsidered the band diagrams taking interfacial dipoles into account. We show that interface dipoles influence the interfacial barrier heights, but not the self-bias, which is only deteremined by the difference in work functions.

[44] X. Lou, M. Zhang, S. Redfern, J. Scott, *Phys. Rev. B* **2007**, *75*, 224104.

[45] This argumentation is applicable if one does not take into account interfacial dipoles, arising from a finite distance between the polarization and screening charges, in constructing the band diagrams. In the Supporting Information, we have redone the analysis including the presence of interfacial dipoles. In that case, the LBSO/PZT interfacial barrier height is enhanced by the interfacial dipole formed across the depleted interfacial LBSO layer. However, the barrier height within the reversal domain is strongly reduced, because within the reversal domain the interfacial dipole is reversed in direction and secondly because of the low dielectric constant of this layer, causing a rapid drop of barrier height toward the PZT. The analysis shows that the effective barrier for charge injection is dominated by the value of the dielectric constant of the depleted LBSO layer and to much less extent the interfacial barrier height without interface dipole.